Electrode Properties of Sr-Doped $LaMnO_3$ on Yttria-Stabilized Zirconia

II. Electrode Kinetics

F. H. van Heuveln

Netherlands Energy Research Foundation ECN, 1755 ZG Petten, The Netherlands

H. J. M. Bouwmeester

Department of Chemical Technology, Laboratory of Inorganic Materials Science, University of Twente, 7500 AE Enschede, The Netherlands

ABSTRACT

A series of six cathodes $Sr_{0.15}La_{0.85}MnO_3$ (SLM) on yttria-stabilized zirconia with different morphology of the electrode/electrolyte interface were characterized by ac impedance and dc polarization measurements. It is found that the electrode kinetics at elevated temperature (945°C) are governed by two serial processes. An activation process can be identified to occur at high cathodic overpotential, whereas a transport process competes with charge-transfer at comparatively low overpotential. Attention is drawn to the profound change in the electrocatalytic properties of $Sr_{0.15}La_{0.85}MnO_3$ upon current passage and its influence in elucidation of the interfacial kinetics.

Introduction

Despite a lot of research carried out on manganite perovskite electrodes for use in solid oxide fuel cells, including thermal and chemical stability, the rate-determining step(s) in the reaction mechanisms have not been identified uniquely. It is clear that unraveling the mechanism of the cathodic reaction sequence aids in proper design of the electrode material to further improve its performance.

There are many aspects which influence electrode performance and hamper identification of the rate-limiting steps. Changes in the microstructure may induce significant changes in electrode performance. This clearly emphasizes the importance of electrode processing conditions. Reaction products like $LaZr_2O_7$ and $SrZrO_3$ can occur at the immediate interface of electrode particle grains and the electrolyte during cofiring. Another important parameter imposed by the microstructure is the three-phase boundary area (TPB area) between the gas, electrolyte, and electrode. It is generally assumed that the reaction rate is proportional with the magnitude of the TPB area available for the oxygen reduction process.

Uncertainty in the interpretation of experimental data also arises from the possible involvement of oxygen ion transport through the oxide electrode. That is, for mixed ionic-electronic conducting electrodes it is envisaged that oxygen ions may be supplied to the electrolyte/electrode interface through the bulk electrode as well as along the electrode surface to the TPB area.[1] In this way, large oxygen fluxes may be sustained and the losses associated with electrode polarization will be less compared with electrode materials where the electrode reaction is restricted to the TPB area. An example of the latter behavior includes the kinetics observed on noble metal electrodes deposited on stabilized zirconia. Hammouche *et al.*[2] and Siebert *et al.*[3] made clear that the performance of Sr-doped $LaMnO_3$ microelectrodes on YSZ is very similar to that of platinum at low polarization values. However, at high cathodic overpotential a significant reduction in polarization loss was observed. The latter observation was interpreted to reflect the contribution of bulk lattice diffusion owing to increased oxygen deficiency of the perovskite electrode

In Part I of this paper, we found the spatial extension of the TPB zone of tape-casted $Sr_{0.15}La_{0.85}MnO_3$ electrodes on stabilized zirconia to be very restricted. Values below 0.05 μm were deduced from measurements of the current constriction in the electrolyte. In the present work, we mainly concentrate on the relationship between electrode kinetics and the interface microstructure based on impedance and i-V measurements.

Theory

Single rate-determining step.—The overall oxygen electrode reaction occurring at the interface between the electronically conducting SLM and the ionically conducting zirconia can be represented by (in Kröger-Vink notation)

$$O_2\,(g) + 4e^- + 2V_O^{\cdot\cdot} \rightarrow 2O_O^x \qquad [1]$$

where $V_O^{\cdot\cdot}$ and O_O^x refer to vacancies and oxygen ions in the electrolyte, respectively. This reaction has been recognized to involve a series of consecutive steps including, *e.g.*, dissociation, charge-transfer, and diffusion of oxygen intermediate species. The Butler-Volmer equation has been adapted for multistep electrode kinetics by Bockris and Reddy[4] to read

$$i = i_0[\exp(\alpha_a f\eta) - \exp(-\alpha_c f\eta)] \qquad [2]$$

in which i is the current, i_0 the exchange current density, η the overpotential, α_a and α_c are the apparent anodic and cathodic charge-transfer coefficients, respectively, and $f = F/RT$. Parameters R, T, and F have their usual meaning. Even though Eq. 2 was originally derived to model charge-transfer kinetics, it also holds when charge-transfer is not the rate-determining step (rds), as demonstrated here. The basic assumption made is that there is a single rds while all other steps have attained virtual equilibrium. Within this approximation it can be shown that[5]

$$\alpha_a = \frac{\gamma_a}{\nu} + r - r\beta \qquad [3]$$

$$\alpha_c = \frac{\gamma_b}{\nu} + r\beta \qquad [4]$$

in which γ_b and γ_a are the respective number of electrons that are transferred before and after the rds, β the symmetry coefficient, and r is the number of electrons in the rds. The stoichiometric number, ν, is the number of times the rds occurs for one act of the overall reaction. From Eq. 3 and 4 it follows that

$$\alpha_a + \alpha_c = r + \frac{\gamma_b + \gamma_a}{\nu} = \frac{n}{\nu} \qquad [5]$$

where n is the total number of electrons involved in the reaction. For the overall oxygen electrode reaction $n = 4$.

At low η ($<< RT/F$) Eq. 2 can be linearized (low field approximation), yielding

$$i = i_o(\alpha_a + \alpha_c)f\eta \quad [6]$$

The value of η/i is referred to as the electrode resistance R_{el}.

Two rate-determining steps.—The oxygen electrode reaction (Eq. 1) may be taken to be made up of several steps, each of which may be rate-determining. Possible schemes for the electrode reaction that were used for the analysis of experimental data are given in Table I. In what follows, the i-η relationship is derived when two consecutive steps are rate-determining. Basic assumptions made in the derivation are: (*i*) the electrode kinetics are governed by two serial processes; (*ii*) microscopic reversibility, *i.e.*, the sequences of reaction steps for both forward and backward reactions are the same; (*iii*) adsorption of oxygen and/or intermediate species is described by a Langmuir-type isotherm, with no overlapping coverages; and (*iv*) any transport of species occurs by a process of pure diffusion, *i.e.*, terms related to electrical migration of species either do not appear or are supposed to be included in the expression describing the diffusional holdup. To simplify the derivation low coverage of adsorbed or intermediate oxygen species is assumed. This implies that the concentration of adsorption sites in the relevant reaction kinetics can be left out of consideration.

The rate equations corresponding to the proposed reaction steps in Model 1 are

$$r_1 = k_1 pO_2 - k_1^- a_{O_{ad}^-}^2 \quad [7]$$

$$r_2 = k_2 aO_{ad} \exp\left(-\frac{1}{2}fE\right) - k_2^- a_{O_{ad}^-} \exp\left(\frac{1}{2}fE\right) \quad [8]$$

$$r_3 = k_3 a_{O_{ad}^-} - k_3^- a_{O_{TPB}^-} \quad [9]$$

$$r_4 = k_4 a_{O_{TPB}^-} \exp\left(-\frac{1}{2}fE\right) - k_4^- \exp\left(\frac{1}{2}fE\right) \quad [10]$$

where k_i and k_i^- are the respective rate constants for the forward and backward reaction. The activities of $V_O^{\cdot\cdot}$ and O_O^x in the electrolyte are taken to be constant, and E is the electrode potential. The symmetry coefficient, β, is taken to be 1/2. If step 2 is assumed to be rate-determining, thus steps 1, 3, and 4 are in virtual equilibrium, then it follows from Eq. 7 that

$$a_{O_{ad}} = \left(\frac{k_1}{k_1^-}\right)^{\frac{1}{2}} pO_2^{\frac{1}{2}} \quad [11]$$

and from Eq. 10

$$a_{O_{TPB}^-} = \left(\frac{k_4^-}{k_4}\right) \exp(fE) \quad [12]$$

Table I. Selected reaction models for oxygen reduction at the SLM/YSZ interface and possible rate-determining steps, and the apparent anodic and cathodic charge-transfer coefficients, α_a and α_c, in case the given steps are rate-determining.

Model Step	Equation	α_a	α_c
Model 1			
1	$O_2(g) \rightarrow 2\ O_{ad}$		
2	$O_{ad} + e \rightarrow O_{ad}^-$	3/2	1/2
3	$O_{ad}^- \rightarrow O_{TPB}^-$	1	1
4	$O_{TPB}^- + e + V_O^{\cdot\cdot} \rightarrow O_O^x$		
Model 2			
1	$O_2(g) + e \rightarrow O_{2,ad}^-$	7/2	1/2
2	$O_{2,ad}^- + e \rightarrow 2\ O_{ad}^-$		
3	$O_{ad}^- \rightarrow O_{TPB}^-$	1	1
4	$O_{TPB}^- + e + V_O^{\cdot\cdot} \rightarrow O_O^x$		
Model 3			
1	$O_2(g) + e \rightarrow O_{2,ad}^-$	7/2	1/2
2	$O_{2,ad}^- \rightarrow O_{2,TPB}^-$	3	1
3	$O_{2,TPB}^- + e + V_O^{\cdot\cdot} \rightarrow O_O^x + O_{ad}$		
4	$O_{ad} + e \rightarrow O_{ad}^-$		
5	$O_{ad}^- + e + V_O^{\cdot\cdot} \rightarrow O_O^x$		

Substitution of this expression into Eq. 9 gives

$$a_{O_{ad}^-} = \left(\frac{k_3^-}{k_3}\right)\left(\frac{k_4^-}{k_4}\right) \exp(fE) \quad [13]$$

Substitution of both Eq. 11 and 13 into rate Eq. 8 gives the reaction rate at steady state which, when converted to a current ($i = -nFr$), reads

$$i = i_{anodic} - i_{cathodic} \quad [14]$$

$$i_{anodic} = nFk_2^-\left(\frac{k_3^-}{k_3}\right)\left(\frac{k_4^-}{k_4}\right) \exp\left(\frac{3}{2}fE\right) \quad [15]$$

$$i_{cathodic} = nFk_2\left(\frac{k_1}{k_1^-}\right)^{\frac{1}{2}} p_{O_2}^{\frac{1}{2}} \exp\left(-\frac{1}{2}fE\right) \quad [16]$$

In equilibrium the net current is zero, *i.e.*, $i_{cathodic} = i_{anodic} \equiv i_o$, which yields the Nernst relation

$$E_{eq} = \text{const} + \frac{RT}{4F} \ln p_{O_2} \quad [17]$$

Hence

$$i_2 = i_{o,2}\left[\exp\left(\frac{3}{2}f\eta\right) - \exp\left(-\frac{1}{2}f\eta\right)\right] \quad [18]$$

where $\eta = E - E_{eq}$ by definition. Note that Eq. 18 is consistent with Eq. 2 for $\alpha_c = 1/2$, $\alpha_a = 3/2$, and $n/\nu = 2$. The exchange current density, $i_{o,2}$, expresses the balanced faradaic activity at equilibrium. Substitution of the Nernst relation into either Eq. 15 or 16 yields $i_{o,2} \propto p_{O_2}^{3/8}$ (for low coverage).

Instead of step 2 we now consider step 3 as rate-determining in Model 1. On assuming that steps 1, 2, and 4 are in virtual equilibrium, substitution of Eq. 11 in rate Eq. 8 gives

$$a_{O_{ad}^-} = \left(\frac{k_2}{k_2^-}\right)\left(\frac{k_1}{k_1^-}\right)^{\frac{1}{2}} p_{O_2}^{\frac{1}{2}} \exp(-fE) \quad [19]$$

Substituting this expression and that for $a_{O_{TPB}^-}$ (Eq. 12) into Eq. 9 we obtain for the corresponding current

$$i_3 = nFk_3^-\left(\frac{k_4^-}{k_4}\right) \exp(fE) - nFk_3\left(\frac{k_2}{k_2^-}\right)\left(\frac{k_1}{k_1^-}\right)^{\frac{1}{2}} p_{O_2}^{\frac{1}{2}} \exp(-fE) \quad [20]$$

In the same way as was shown previously, the relation between current, i, and the overpotential, η, can be written as

$$i_3 = i_{o,3}[\exp(f\eta) - \exp(-f\eta)] \quad [21]$$

If we repeat the argument for the exchange current density it follows that $i_{o,3} \propto p_{O_2}^{1/4}$ (for low coverage). It should be noted that $i_{o,3}$ and the transfer coefficients in Eq. 21 only bear a formal significance, since in deriving this equation the charge-transfer reaction is assumed to be infinitely fast. The electrode process is governed by step 3 (Eq. 9), which represents the limited transport of O_{ad}^- species to the TPB area. Accordingly, rate constants k_3 and k_3^- reflect the ratio of a diffusion coefficient over an effective distance in accordance with Fick's first law of diffusion. Note further that Eq. 21 does not predict a limiting current at high values of η, which is due to the potential dependency of the O_{ad}^- concentration, as seen from Eq. 12 or 13. The effect of increasing η, whatever the polarization direction, is to increase the gradient in concentration of O_{ad}^- species. The transport limitation disappears in the limit of high values of η.

Under condition of combined activation and transport control, *i.e.*, assuming reaction steps 2 and 3 to be both

rate-determining, the solution obtained on a steady-state basis reads

$$i = i_{\text{anodic}} - i_{\text{cathodic}} \quad [22]$$

with

$$i_{\text{anodic}} = \frac{i_{o,2} \exp(\alpha_{a,2} f\eta) i_{o,3} \exp(\alpha_{a,3} f\eta)}{i_{o,2} \exp(\alpha_{a,2} f\eta) + i_{o,3} \exp(\alpha_{a,3} f\eta)} \quad [23]$$

$$i_{\text{cathodic}} = \frac{i_{o,2} \exp(-\alpha_{c,2} f\eta) i_{o,3} \exp(-\alpha_{c,3} f\eta)}{i_{o,2} \exp(-\alpha_{c,2} f\eta) + i_{o,3} \exp(-\alpha_{c,3} f\eta)} \quad [24]$$

A similar equation may be derived when considering Models 2 and 3. Subscripts should be replaced then by the appropriate quantities listed in Table I.

Experimental

A $Sr_{0.15}La_{0.85}MnO_3$ (SLM) powder batch was divided into two portions. One portion was attrition milled for 5 h, and the other one remained unmilled. Cathodes of the two portions were prepared by suspending the powders followed by tape casting on presintered YSZ electrolyte disks. The cathodes with corresponding labels are listed in Table II. The contact diameter of SLM particles on YSZ and the total SLM coverage were determined by scanning electron microscopy (SEM) and are presented in Table III. A full description of the microstructural investigations is presented in Part I of this study.[6]

The scheme of electrochemical measurements is shown in Fig. 1. At 950°C a constant current, i, of 100 mA/cm^2 was applied to the cathode/electrolyte samples for a known period between 30 and 90 min. Then the electrode potential was decreased stepwise to zero. In this way the i-V characteristic was obtained. Immediately hereafter the impedance was measured, and again after 30 min in order to study the relaxation behavior of the electrode. Analysis of the impedance diagrams was done by nonlinear least squares fitting the impedance of an equivalent circuit to the experimental data.[7] Data were corrected for the inductance of the measurement leads. Analysis of the i-η curves was performed by nonlinear least squares fitting of either Eq. 2 or 22 to the experimental data. Electrode potentials were corrected for the iR_o drop of the electrolyte yielding the electrode overpotentials η. Details of the measurement setup and equipment are given in Part I.[6]

Table II. Cathode types, sintering temperatures (sintering time 1 h), and corresponding labels used in this report.

Cathode type	Sintering temperature (°C)	Label
$Sr_{0.15}La_{0.85}MnO_3$	1100	U-11[a]
	1200	U-12
	1300	U-13
$Sr_{0.15}La_{0.85}MnO_3$	1100	M-11[b]
	1200	M-12
	1300	M-13

[a] Cathodes prepared from unmilled powder.
[b] Cathodes prepared from milled powder.

Table III. Values for the total contact surface area, D_c (relative to the geometrical electrode area), the electrolyte thickness, l, the electrode thickness, t, the mean grain diameter, d_g, and the mean particle contact diameter, d_c, of the SLM particle on YSZ.[a]

Label	D_c (±10%) (%)	l (±5 μm) (μm)	t (±5 μm) (μm)	d_g (±15%) (μm)	d_c (±15%) (μm)
U-11	12	125	65	0.29	0.19
U-12	13.5	130	60	0.63	0.41
U-13	15	133	57	0.83	0.58
M-11	14	137	60	0.29	0.19
M-12	33	130	55	0.90	0.75
M-13	58	127	46	2.0	1.82

[a] Results discussed in Part I of this study, Ref. 6.

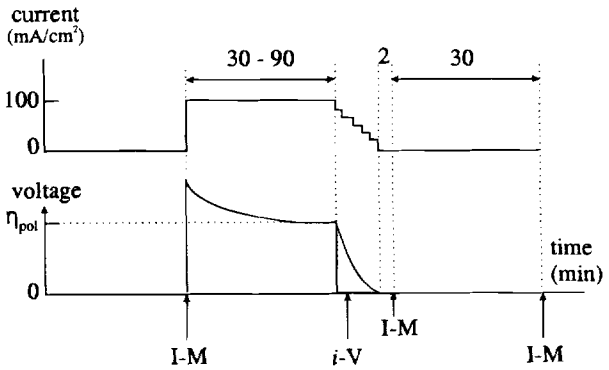

Fig. 1. Schematic diagram of the measurement procedure. I-M refers to impedance and i-V to current voltage measurement. The steady-state overpotential during passage of 100 mA/cm^2 is denoted as η_{pol}.

Results

Impedance spectra, taken at 945°C before and 2 and 30 min after polarizing the sample, are shown in Fig. 2. All data could be fitted to an equivalent circuit consisting of two parallel branches (RC) and (RQ). Both branches are in series and in series with a resistor R and inductor L. C is a capacitor and Q is a constant phase element (CPE). No low-frequency inductive loops were observed within the used frequency range (1 Hz to 1 MHz). The resulting circuit is shown in Fig. 3 and is depicted by the circuit description code $R_0L(R_1C)(R_2Q)$.[8] L represents the inductance of the measurement leads and was found to vary between 5×10^{-8} and 8×10^{-8} H. Values for the fit parameter χ^2 varied between 10^{-4} and 10^{-6}, indicating reliable fitting. Values for the circuit parameters obtained by fitting the impedance data before and 2 min after current passage are listed in Table IV. As can be seen from this table, the most significant changes upon current passage are observed for R_2 for the unmilled series. Experimental and fitted data of impedance measurements taken 2 min after the current passage are shown in Fig. 4. Cathodic polarization curves of the two cathode types, U-11···U-13 and M-11···M-13, are shown in Fig. 5. These Tafel plots were fitted to Eq. 22.

Discussion

Impedance analysis.—The equivalent circuit that fits the impedance data, as shown in Fig. 3, suggests that there are two serial processes involved in the electrode reaction. Both are represented by two separate parallel branches (R_1C) and (R_2Q). The resistance R_1 is interpreted as the charge-transfer resistance R_{ct} and the capacitance C as the double-layer capacitance C_{dl}. Figure 6 shows that C_{dl} increases with increasing surface coverage of SLM on YSZ, as expected and also found by others.[9] The (R_2Q) branch may be related to another process such as adsorption or diffusion. As can be seen from Table IV, the value of the CPE exponent n varies between 0.5 and 0.8. A value of 1 corresponds to a pure capacitance, whereas as value of 0.5 is found for a Warburg element describing semi-infinite diffusion behavior.

Current-voltage measurements.—Cathodic polarization curves are shown in Fig. 5. A strong influence of the electrode microstructure is observed. As discussed in Part I of this paper,[6] the steady-state overpotential η_{pol} (at 100 mA/cm^2) is found inversely proportional with the magnitude of A_{cs}. The latter quantity is determined by the electrode microstructure and is taken as a measure for the available TPB area. An overall fit of the polarization curves to Eq. 2, *i.e.*, assuming a single rds, resulted in frac-

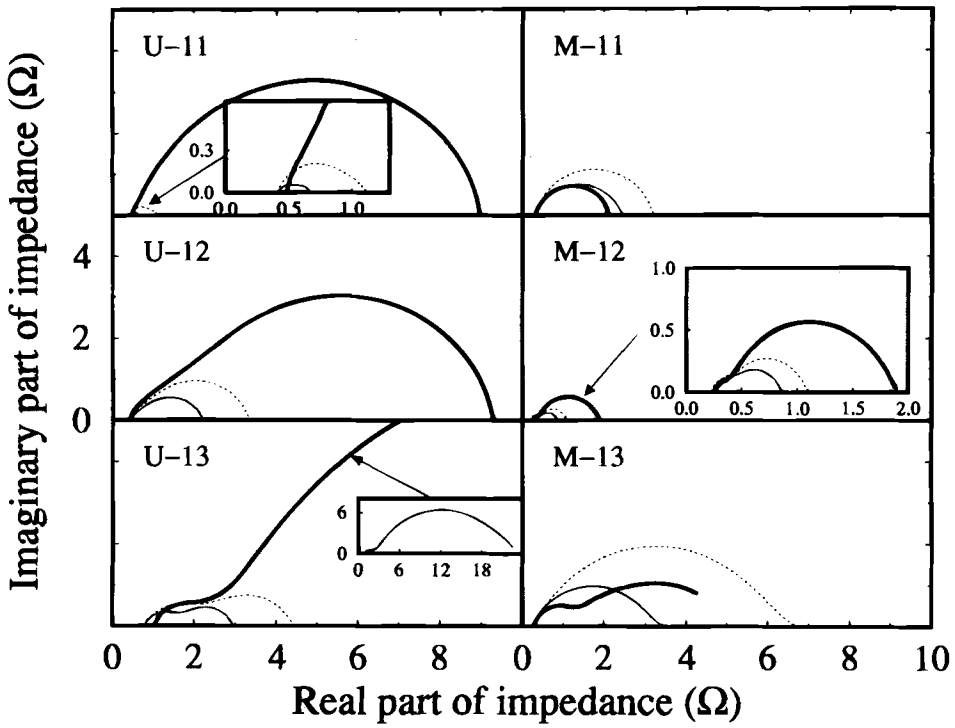

Fig. 2. Impedance diagrams (at zero polarization) before and after passing a dc current of 100 mA/cm² for 30 to 90 min through different SLM cathode types on YSZ. See Table II for explanation of labels. For scaling reasons the inductive tails at high frequency are not shown. Measurements were taken at 945°C, before (bold line), 2 min after (thin line), and 30 min after (dotted line) passing a current of 100 mA/cm² for 30 min.

tional values of α_c between 0.6 and 1.3 for the different cathodes under the condition that $\nu = 2$. A reasonable fit (not shown) was obtained only for a limited range in overpotential ($\eta < 150$ mV). On the other hand, a value of $\alpha_c = 0.5$ can be extracted from the Tafel slope at high overpotentials. The observed behavior, however, reflects the contribution of at least two competing rate-determining steps in the electrode kinetics, *i.e.*, in agreement with the results from impedance measurements.

Improved fits of the polarization curves were obtained assuming the rate of the electrode reaction to be controlled by combined charge-transfer and diffusion of singly charged oxygen species. In the search for possible electrode reaction models we were guided by the fact that the Tafel slope indicates $\alpha_c = 1/2$ at high cathodic overpotentials and that no diffusion limiting current occurs. The value of $\alpha_c = 0.5$ points to electron transfer either to adsorbed oxygen molecules or to oxygen adatoms. This process is predominant at high overpotentials. It was further assumed that in an elementary step only one electron transfer can take place at a time and that the interfacial kinetics are predominantly governed by processes occurring on the electrode surface rather than on the electrolyte. Several electrode reaction models were considered, and the ones which are most feasible to fit the experimental data are presented in Table I. The experimental i-η curves were fitted to Eq. 22 with the appropriate values of α_a and α_c for each of the models listed in Table I. The best least squares fit was obtained for Model 1. The experimental and fitted data are given in Fig. 5. The values for the exchange current density, i_o, obtained by fitting are given in Table V. The electrode kinetics can thus be described by charge-transfer and a diffusional process in which O^-_{ad} species are involved. It is clear that both processes will contribute to the total electrode resistance. Any current limitation due to the adsorption or surface diffusion of neutral oxygen or intermediate species is believed to occur at higher overpotentials than used in our experiments.

Using Eq. 6, which holds also as a low field approximation for Eq. 22 through 24, the resistive contributions of both rate-determining steps can be calculated. These are compared with the values obtained from impedance measurements performed immediately after recording the i-η curve. The results are given in Fig. 7. A very good agreement is noted for the charge-transfer resistance obtained by the two techniques. That for the diffusive process is less ideal. This is in part related to the relaxation behavior of the electrodes observed after dc current passage. That is, the disagreement observed for selected electrodes corresponds with the direction in which the impedance relaxes (Fig. 2) after dc current passage.

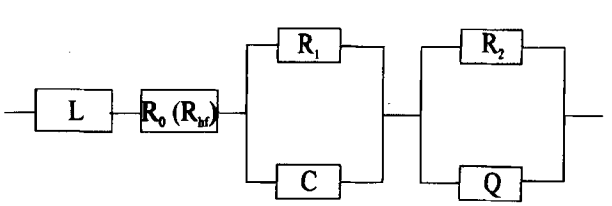

Fig. 3. Equivalent circuit used to fit the data from impedance measurements. *R* is resistance, *C* is capacitance, and *Q* a constant phase element. The inductance *L* is due to the measurement leads.

Table IV. Parameters obtained from fitting the impedance data (Fig. 4) to the equivalent circuit shown in Fig. 3. Values for different cathode types are given 2 min before (b) and after (a) passing a current of 100 mA/cm² for 30 to 90 min.[a]

Sample code	R_0 (Ω)	R_1 (Ω)	C (F)	R_2 (Ω)	Q (CPE) ($s^n\ \Omega^{-1}$)	n (CPE)
U-11-b	0.321	0.18	5.0E-6	8.48	3.8E-5	0.83
U-11-a	0.222	0.20	7.6E-6	0.18	4.8E-3	0.67
U-12-b	0.390	0.50	6.0E-6	8.80	3.4E-4	0.72
U-12-a	0.327	0.21	9.7E-6	1.65	3.8E-4	0.75
U-13-b	0.510	1.05	1.3E-6	20.8	7.2E-4	0.68
U-13-a	0.403	0.46	3.7E-6	1.70	2.8E-3	0.62
M-11-b	0.279	0.05	7.2E-5	1.76	1.4E-4	0.87
M-11-a	0.281	0.22	2.4E-4	1.85	2.6E-4	0.77
M-12-b	0.252	0.12	6.4E-5	1.61	3.1E-3	0.79
M-12-a	0.218	0.23	8.9E-5	0.41	2.1E-3	0.68
M-13-b	0.260	0.61	2.3E-4	7.50	3.7E-2	0.51
M-13-a	0.366	0.75	1.3E-3	3.33	1.4E-4	0.69

[a] Values for the indicator L are not given.

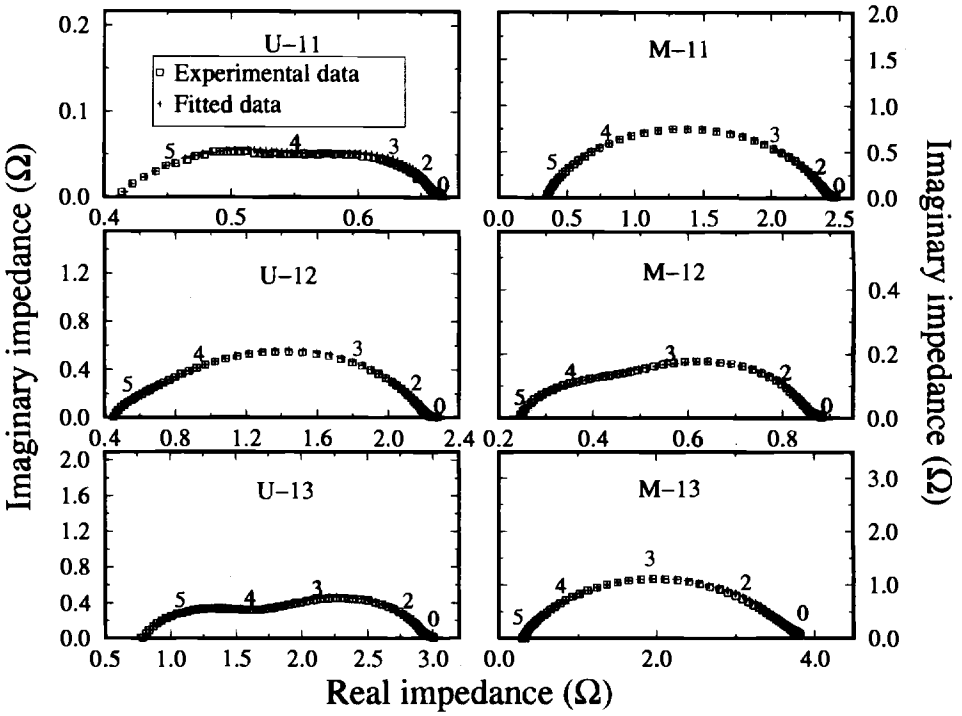

Fig. 4. Experimental and fitted impedance diagrams (at zero polarization) for different SLM cathode types on YSZ. See Table II for explanation of labels. Numbers 0 to 5 indicate the logarithm of the frequency (Hz). Data was fitted to the circuit shown in Fig. 3. Measurements were taken at 945°C, 2 min after passing a dc current of 100 mA/cm² for 30 to 90 min.

Interfacial kinetics.—Our modeling indicates that oxygen reduction on SLM/YSZ can be described by electron transfer mediated by SLM to either dissociative-adsorbed or associative-adsorbed oxygen (O_{ad}, $O_{2,ad}$), proceeded by diffusion of the formed intermediate species along the electrode surface toward the TPB region. It thus follows that there is a strong resemblance to the kinetics of porous Pt electrodes under low cathodic overpotential, as has also been suggested by others.[3] Models used for the analysis of experimental data are visualized in Fig. 8. The spatial extension beyond the TPB line can be explained by spill-over of oxygen electroactive species along the electrolyte surface. Our analysis, in which it is assumed that the reaction zone forms a ring around the electrode particle grain, suggests that the TPB extension is limited to values below 0.05 μm (see Part I). Since the electronic conductivity of zirconia is known to be very small, the spill-over mechanism most likely deals with fully ionized oxygen species O^{2-}_{ad}. Even though this is not indicated in Fig. 8, the latter species may be formed by electron transfer from SLM to, *e.g.*, O^{-}_{ad} upon arrival at the TPB. This step is mediated either by SLM or electrocatalytic domains formed by the diffusion of manganese ions into YSZ.[10] Furthermore, since SLM at conditions covered by this experiment is a poor ionic conductor, it is expected that transport of oxygen through the bulk electrode does not make a significant contribution to the overall oxygen flux. At the maximum current density of 100 mA/cm² used in our experiments, the lateral extension of the TPB area under the electrode grain is likely to be relatively small.

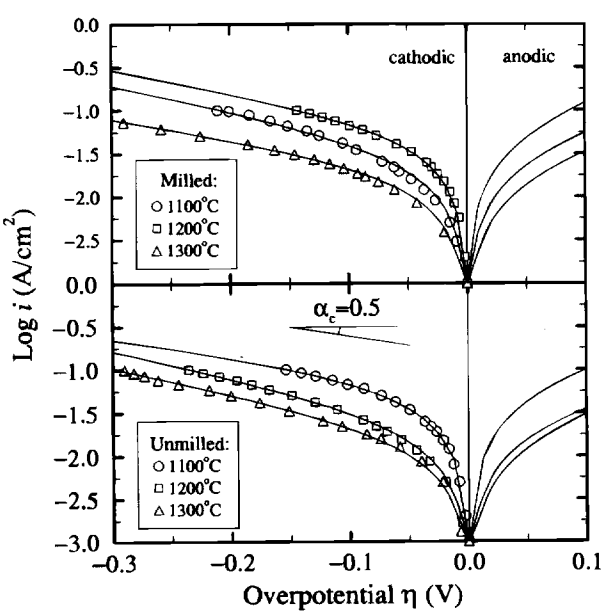

Fig. 5. Tafel plots for SLM electrodes prepared from unmilled (bottom) and milled powder (top), sintered at 1100, 1200, and 1300°C. Measurements were carried out at 945°C in air. The lines represent the fit to Eq. 22 based on Model 1.

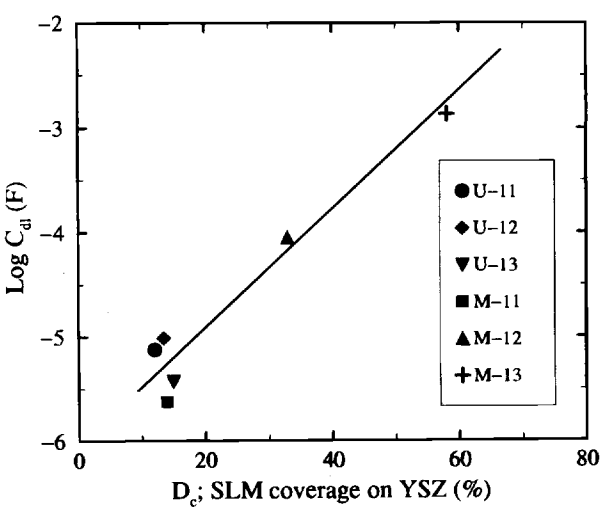

Fig. 6. Plot of the logarithm of the double-layer capacitance C_{dl} vs. the SLM surface coverage on YSZ.

Table V. Apparent exchange current densities $i_{o,2}$ and $i_{o,3}$ for Model 1 (see Table I) obtained from fitting Eq. 22 to the cathodic polarization curves.

Label	$i_{o,2}$ (mA cm^{-2})	$i_{o,3}$ (mA cm^{-2})
U-11	67 (6)	103 (6)
U-12	77 (5)	19 (4)
U-13	44 (4)	14 (6)
M-11	113 (4)	20 (4)
M-12	83 (5)	78 (3)
M-13	22 (7)	19 (6)

Effect of current passage.—The sequence of the electrochemical measurements was discussed in the Experimental section. The overpotential, η, during passage of a 100 mA/cm^2 dc current at 945°C was found to change with time and becomes invariant within approximately 30 min. This change is reflected in the impedances of each of the electrode specimens. Spectra were recorded before and 2 and 30 min after current passage. As seen from Fig. 2, a drastic decrease of the electrode resistance is found for the unmilled cathode series. The impedances measured 30 min after switching off the current show that the impedance characteristics relaxes to that before current passage. Approximately 2 to 3 h are required to reestablish the condition as seen before current passage. Less pronounced changes upon current passage were found for the milled cathode series, which also showed a relaxation behavior different from that of the unmilled series.

Similar phenomena have been observed by others. According to Tsukuda and Yamashita,[11] the electrode properties of screen-printed $La_{0.8}Sr_{0.2}MnO_3$ electrodes on YSZ before and after dc polarization can be correlated with an apparent change in microstructure. A dc current of 500 mA/cm^2 during 18.5 h was fed through the cell maintained at 1000°C. Using SEM, the authors deduced an increase in effective TPB length from the change in microstructure of several tens of percent. No report was made of any relaxation behavior after current passage.

In the present study, we were not able to detect any change in the microstructure of electrode specimens induced by the current passage. Since the electrode impedance is restored to its initial state 2 to 3 h after current passage, we consider it unlikely that the observed phenomena are caused by changes in the microstructure. Moreover, if the measurement sequence as shown in Fig. 1 was performed again, the same relaxation phenomena were observed. On the other hand, it cannot be excluded that the results obtained by Tsukuda and Yamashita are related to the high current of 500 mA/cm^2 and that due to the lower current density in this study these microstructural changes are not observed.

Table IV shows that for the unmilled electrode series, the change in the value of the circuit parameter R_2 (R_d) induced by current passage is more significant than that of the other circuit parameters. Therefore, in view of the present modeling, the improved electrode performance upon current passage can be attributed to enhanced diffusion of intermediate oxygen species (model 1, step 3). For the milled electrode series the changes induced by current passage are less pronounced. Since the main difference between both electrode series concerns the nature of the contact (see Fig. 4 of Part I), this seems to play a decisive role in the diffusion process. However, the precise mechanism of this enhancement remains unclear. Clearly more research is needed in interpreting the phenomena observed upon current passage, but it may be noted that erroneous conclusions can be drawn, *e.g.*, from the analysis of impedance diagrams when the effect of current passage is not taken into account.

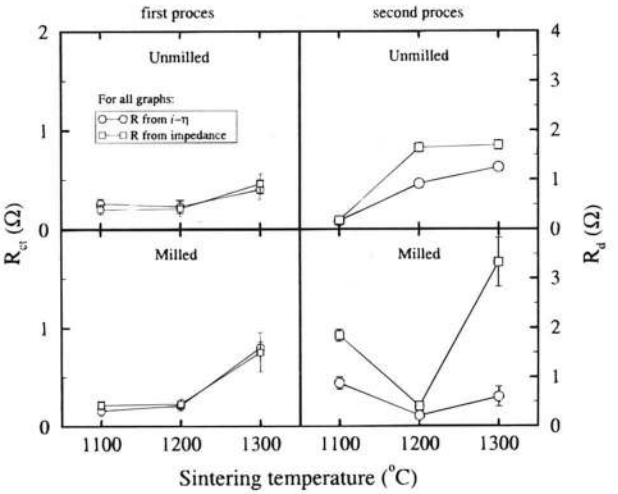

Fig. 7. Correlation between the resistances R_{ct} and R_d as determined from impedance measurements and calculated from $i_{o,2}$ and $i_{o,3}$ as obtained by modeling the i-η curves. (left column) activation process, (right column) transport process, (upper row) results for unmilled cathode, and (bottom row) results for milled cathode.

Conclusions

1. Cathodic reduction at the moderate overpotentials used in our experiments involves a combined activation-diffusion process. Diffusion of O^-_{ad} species along the SLM surface to the TPB area is presumed to compete with charge-transfer at low overpotential. The diffusion limitation disappears at high cathodic overpotentials. The results from modeling the i-V characteristics are consistent with impedance data, suggesting that both processes act in series.

2. Cathodic polarization with a constant current of 100 mA/cm^2 significantly alters the impedance response of SLM electrodes on YSZ. The response is recovered after

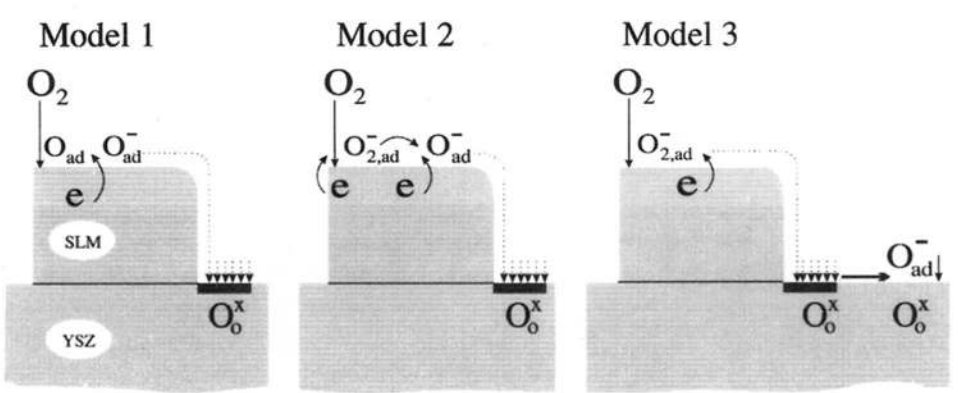

Fig. 8. Visualization of the reaction models listed in Table I for oxygen reduction at the SLM/YSZ interface. Model 1 was found to give the best fit results. The dark shaded area is drawn to indicate a spatial extension of the TPB zone.

several hours, which rules out the possibility that changes in the electrocatalytic properties of SLM on YSZ are due to changes in the microstructure of the electrodes.

3. Results from modeling indicate that it is mainly the diffusion process which is influenced by the current treatment.

Acknowledgments

This work was supported in part by the Commission of the European Communities in the framework of the JOULE program (Contract JOU2-CT92-0105). The authors acknowledge Dr. S. B. van der Molen for critical reading of the manuscripts.

Manuscript submitted April 25, 1996; revised manuscript received Sept. 11, 1996.

The Netherlands Energy Research Foundation ECN assisted in meeting the publication costs of this article.

LIST OF SYMBOLS

A_{cs} electrolyte effective cross-sectional area used as a relative measure for the TPB area
A_{geo} geometric electrode area
C_{dl} double-layer capacitance
d_c mean contact diameter of a particle at interface
d_g mean diameter of a particle in the electrode at the interface
D_c total contact surface area at the interface
F Faraday constant, 96, 487 C/eq
i current density
k reaction constant
n exponent of the constant phase element
Q symbol presentation for constant phase element
r reaction rate
R gas constant
R_{ct} charge-transfer resistance
R_{hf} high-frequency intercept on the real-axis in the impedance diagram
R_o electrolyte resistance
T temperature

Greek

η overpotential (after correction of iR drop)
η_{pol} overpotetntial at the end of a constant current passage of 100 mA/cm^2 for 30 min

REFERENCES

1. B. C. H. Steele, *Solid State Ionics*, **86-88**, 1223 (1996).
2. A. Hammouche and E. Siebert, A. Hammou, and M. Kleitz, *This Journal*, **138**, 1212 (1991).
3. E. Siebert. A. Hammouche, and M. Kleitz, *Electrochim. Acta*, **40**, 1741 (1995).
4. J. O'M. Bockris and A. K. N. Reddy, *Modern Electrochemistry*, Vol. 2, Plenum Press, New York (1977).
5. J. O'M. Bockris and S. U. M. Khan, *Surface Electrochemistry, A Molecular Level Approach*, p. 221, Plemum Press, New York (1993).
6. F. H. van Heuveln, H. J. M. Bouwmeester, and F. P. F van Berkel, *This Journal*, **144**, 126 (1997).
7. B. A. Boukamp, Equivalent Circuit, A software program for ac immittance data analysis, Version 4.51, University of Twente, The Netherlands (1992).
8. B. A. Boukamp, *Solid State Ionics*, **20**, 31 (1986).
9. J. Mizusaki, H. Tagawa, K. Tsuneyoshi, and A. Sawata, *This Journal*, **138**, 1867 (1991).
10. K. Ravindranathan Thampi, A. J. McEvoy, and J. Van Herle, *This Journal*, **142**, 506 (1995).
11. H. Tsukuda and A. Yamashita, *Proceedings of the First European Solid Oxide Fuel Cell Forum*, October 3-7, 1994, Lucerne, Switzerland, U. Bossell, Editor, pp. 715-724. European SOFC Forum, Baden, Switzerland (1994).

Electrochemical Study of the Properties of Indium in Room Temperature Chloroaluminate Molten Salts

Julia Shin-Yu Liu and I-Wen Sun*

Department of Chemistry, The National Cheng-Kung University, Tainan, Taiwan

ABSTRACT

The electrochemistry of indium was studied with voltammetry and chronoamperometry at glassy carbon, tungsten, and nickel electrodes in the basic and acidic aluminum chloride-1,2-dimethyl-3-propylimidazolium chloride molten salt at 27°C. In the basic melt, In(III) is complexed as $[InCl_5]^{2-}$, which could be reduced to indium metal through a three-electron reduction process. The electrodeposition of indium on glassy carbon and tungsten electrodes involves progressive three-dimensional nucleation on a finite number of active sites with diffusion-controlled growth of the nuclei. The electrodeposition of indium metal on a nickel electrode entails progressive three-dimensional nucleation on a large number of active sites. The formal potentials of the In(III)/In couple in the 44.4 to 55.6 and 49.0 to 51.0 mole percent (m/o) melts are −1.096 and −1.009 V, respectively, *vs.* Al(III)/Al in the 66.7 to 33.3 m/o.

Room temperature chloroaluminate molten salts are obtained from mixtures of anhydrous aluminum chloride with organic quaternary ammonium chloride salts.[1] The most popular examples are those from mixing $AlCl_3$ with N-butylpyridinum chloride(n-BPC)[2] or 1-ethyl-3-methylimidazolium chloride (EMIC).[3] These molten salts have proven to be versatile solvents for chemical and electrochemical processes. One of the attractive properties of these melts is their adjustable Lewis acidity[4] which can be altered by varying the molar ratio of $AlCl_3$ to organic chloride salt. Basic melts contain a molar excess of organic chloride, whereas acidic melts contain an excess of $AlCl_3$. It is well known that the chemistry and electrochemistry of many elements are influenced significantly by the Lewis acidity of the melt.[5]

The addition of substituent to the pyridinum or imidazolium ring has been shown to cause a shift in reduction potential for the pyridinium or imidazolium cation.[6] Based on this approach, Gifford and Palmisano[7] prepared the 1,2-dimethyl-3-propylimidazolium chloride (DMPIC) room temperature melt. The cathodic electrochemical limit for the basic $AlCl_3$-DMPIC was about 0.5 V more negative than that for basic $AlCl_3$-EMIC. The wider electrochemical window would allow the $AlCl_3$-DMPIC melt to be used as a solvent for the study of redox couples which exhibit redox potentials more negative than the cathodic limit of basic $AlCl_3$-EMIC melts.

For the development of room temperature chloroaluminate melts as electrolytes and as fluids for electroplating, electrowinning, and electrorefining, information about the electrodeposition of metals in these melts is important. A few studies on the electrodeposition of metals from room temperature chloroaluminate melts have been reported. Metals such as aluminum,[8] lead,[9] silver,[10] cobalt,[11] iron,[12] and bismuth[13] were electrodeposited from acidic melts, whereas mercury,[14] copper,[15] gold,[16] antimony,[17] tin,[18] and

* Electrochemical Society Active Member.